



UNIVERSIDADE ESTADUAL DE CAMPINAS
SISTEMA DE BIBLIOTECAS DA UNICAMP
REPOSITÓRIO DA PRODUÇÃO CIENTÍFICA E INTELLECTUAL DA UNICAMP

Versão do arquivo anexado / Version of attached file:

Versão do Editor / Published Version

Mais informações no site da editora / Further information on publisher's website:

<https://aip.scitation.org/doi/10.1063/1.4964429>

DOI: 10.1063/1.4964429

Direitos autorais / Publisher's copyright statement:

©2016 by AIP Publishing. All rights reserved.

DIRETORIA DE TRATAMENTO DA INFORMAÇÃO

Cidade Universitária Zeferino Vaz Barão Geraldo

CEP 13083-970 – Campinas SP

Fone: (19) 3521-6493

<http://www.repositorio.unicamp.br>

Residual stress in nano-structured stainless steel (AISI 316L) prompted by Xe⁺ ion bombardment at different impinging angles

S. Cucatti,¹ R. Droppa, Jr.,² C. A. Figueroa,³ M. Klaus,⁴ Ch. Genzel,⁴ and F. Alvarez^{1,a)}

¹Instituto de Física “Gleb Wataghin”, UNICAMP, 13083-859, Campinas, SP, Brazil

²Centro de Ciências Naturais e Humanas, UFABC, 09210-580, Santo André, SP, Brazil

³CCET, Universidade de Caxias do Sul, 95070-560 Caxias do Sul, RS, Brazil

⁴Helmholtz-Zentrum Berlin für Materialien und Energie, D-12489 Berlin, Germany

(Received 28 July 2016; accepted 25 September 2016; published online 13 October 2016)

The effect of low energy (<1 keV) xenon (Xe⁺) ion bombardment on the residual stress of polycrystalline iron alloy (AISI 316L steel) is reported. The results take into account the influence of the ion incident angle maintaining constant all other bombarding parameters (i.e., ion energy and current density, temperature, and doses). The bombarded surface topography shows that ions prompt the formation of nanometric regular patterns on the surface crystalline grains and stressing the structure. The paper focalizes on the study of the surface residual stress state stemming from the ion bombardment studied by means of the “sin² ψ ” and “Universal Plot” methods. The analysis shows the absence of shear stress in the affected material region and the presence of compressive in-plane residual biaxial stress (~ 200 MPa) expanding up to ~ 1 μ m depth for all the studied samples. Samples under oblique bombardment present higher compressive stress values in the direction of the projected ion beam on the bombarded surface. The absolute value of the biaxial surface stress difference ($\sigma_{11}-\sigma_{22}$) increases on ion impinging angles, a phenomenon associated with the momentum transfer by the ions. The highest stress level was measured for ion impinging angles of 45° ($\sigma_{11} = -380 \pm 10$ MPa and $\sigma_{22} = -320 \pm 10$ MPa). The different stresses obtained in the studied samples do not affect significantly the formation of characteristic surface patterns. *Published by AIP Publishing.* [<http://dx.doi.org/10.1063/1.4964429>]

I. INTRODUCTION

Shot peening process is a procedure used to prompt stress, defects, and plastic deformation on the surface of metals. This cold working process consists in bombarding the metal sample with small steel balls, glass or hard ceramic particles. This treatment improves process involving atomic diffusion species in metals such as nitriding. These effects are due to surface chemical reaction kinetics modification by increasing grain boundary paths obtained on the nanostructured surfaces.¹ Also, low energy ion bombardment (“atomic attrition”) is a technique applied for improving elements incorporation such as nitrogen, carbon, and boron, by physical surface modification. Moreover, the material surface can be tailored by sputtering patterning, erosion, prompting defects, roughness, and stress.^{2–6} Such procedures modify the surface topography, inducing regular and peculiar patterns depending on both material and bombardment conditions.^{7–9}

In surface hardening processes, ion bombardment is currently used, leading to elimination of oxide barriers in metals, improving, for instance, nitrogen diffusion in plasma nitriding applications. Moreover, some studies have shown that the changes induced in materials after bombardment, such as the presence of defects, stress, and roughness, can act beyond surface cleaning by prompting nitrogen diffusion.^{10–14} The physical modification induced by the ion

bombardment involves concomitant effects, such as linear momentum transference, local heating spikes, self-diffusion, atoms re-locations, and sputtering.⁹

These considerations suggest that the modifications introduced by ion bombardment deserve special attention. In particular, the surface topography and the strain introduced by ion bombarding should be examined in order to gain physical insight in nitriding, substrate preparation for wear-resistant, and hard coatings applications. As it is well known, ion bombardment generates compressive stress due to the fact that heavy ions having energies ≥ 100 eV are underneath implanted (knock-on effect).^{15–17} The implanted atoms occupy smaller sites than the usual atomic volume, generating stress parallel and outwards to the sample surface. On one hand, since the sample surface is free to expand in the direction of its normal, the generated stress component in this direction, σ_{33} , is relaxed. On the other hand, a parallel expansion is not allowed by the substrate’s stiffness, generating a macroscopic biaxial stress.^{12,16}

The effect of ion bombarding on the induced stress is well studied in the case of thin films deposited by a variety of techniques, such as sputtering, ion beam assisted deposition, chemical vapor deposition, and ion beam assisted evaporation. Regarding the importance of residual stress in polycrystalline thin films deposition, a comprehensive paper by Chason and Guduru was recently published.¹⁸ Chan *et al.* reported the bombarding effect on the stress as function of the dose in evaporated Pt (platinum) thin films of 15–40 nm grown on crystalline silicon.¹⁹ They found tensile or

^{a)}Author to whom correspondence should be addressed. Electronic mail: alvarez@ifi.unicamp.br

compressive stress depending on the noble gas used for ion bombarding, ion energy, as well as the preparation conditions.

We remark also that the studies of stress dealing with growing film process are not, in general, taking into account the *projectile incident angle*. Indeed, the effect of the projectile incident angle on the substrate is important since ion bombarding is currently employed in the preparation of substrates in coating technological applications. Therefore, in this paper we are explicitly investigating the influence of the ion incident angle on the material residual stress. Specifically, the effects of Xe^+ bombardment on the surface and in depth residual stress prompted in AISI 316L stainless steel are reported as a function of the *ion-impinging angle* at constant ion energy and dose. Both absolute values and depth profile of stress components are discussed considering the transferred momentum as a function of the ion incident angle.

II. EXPERIMENTAL

A. Sample preparation

Rectangular samples (20×10 mm, 2 mm thick) of austenitic stainless steel AISI 316L (nominal composition C: <0.08 , Si: <0.5 P: 0.05, S: 0.03, Mn: 1.6, Mo: 2.1, Ni: 12.0, Cr: 17.0, and Fe: balanced in wt. %) were mirror polished (roughness <1.5 nm). The polishing process followed a standard sequential routine using diamond disc grinding and polishing diamond pastes of 9, 3, and $1 \mu\text{m}$ sizes. Afterward, the samples are bombarded by xenon ions (Xe^+) in a high vacuum chamber (background pressure $<10^{-5}$ Pa) containing ion sources (Kaufman-type, 3 cm diameter beam). The working pressure during Xe^+ bombardment was 1.4×10^{-1} Pa. More details of the apparatus are reported elsewhere.²⁰ The substrates were bombarded during 30 min, at room temperature. The nominal ion current density was fixed at ~ 1.4 mA/cm² and the corresponding dose was 1.6×10^{19} ions/cm². Nominal ion beam energies were fixed at 1 keV for all experiments. Five impinging ion bombardment angles ν were selected for the study ($\nu = 0^\circ, 15^\circ, 30^\circ, 45^\circ, \text{ and } 60^\circ$), where ν is defined as the angle relative to the normal to the sample surface (Figure 1). Calculations using the program TRIM²¹ show that the stopping distance of the ions in these conditions is ~ 1.1 – 1.8 nm. Figure 1 shows both the step

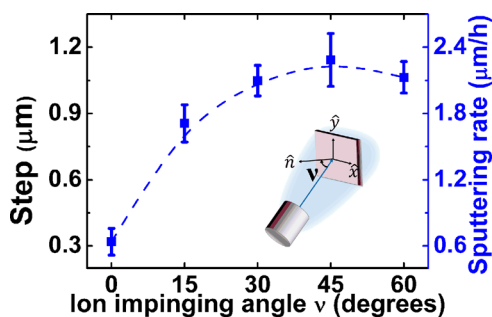


FIG. 1. Step generated after ion bombarding the studied samples (left axis). The calculated sputtering rate as a function of the ion-impinging angle is indicated (right axis). A schematic representation of the ion beam bombarding set up is also shown.

(measured with a profilometer) produced by the bombarding erosion and sputtering rate for the studied impinging angles. Each step value present in Figure 1 corresponds to the average value of five measurements. The error bars correspond to the calculated standard deviation. We note that experiments reported correspond to samples that have lost the memory of the possible effects introduced by the polishing preparation procedure since around $1 \mu\text{m}$ of material have been removed during the treatment (Figure 1). $1 \mu\text{m}$ is just the last size of the polishing diamond paste used in the sample preparation.

The morphology of the surface of the irradiated samples was analyzed by scanning electron microscopy FEG-SEM (Quanta 650FEG) at the Brazilian Nanotechnology National Laboratory – LNNano, Campinas, SP, Brazil.

B. X-ray diffraction and residual stress analysis

In order to study the residual stress prompted by the ion bombarding treatment, the samples were characterized by X-ray diffraction measurements. The measurements were performed in the symmetric ψ -mode (i.e., by tilting the sample around an axis in the diffraction plane) for four equally spaced azimuth angles φ , where $\varphi = 0^\circ$ is the angle coinciding with the direction of the ion bombardment projection on the sample surface. The selected diffraction line for X-ray stress analysis (XSA) was the reflection 311 of austenite at $2\theta = 90.4^\circ$, which is a good compromise between sufficient intensity and the magnitude of the Bragg angle. The latter should be large enough in order to detect without difficulty the strain induced diffraction line shifts given by the expression $\Delta 2\theta = -2\varepsilon \tan \theta$, where ε is the lattice strain.²² The parameters used in the experiments are summarized in Table I. The X-ray measurements were carried out at the *Helmholtz-Zentrum Berlin für Materialien und Energie*, Berlin, Germany.

The individual diffraction lines were evaluated by least squares fitting of the data using a pseudo-Voigt function. The data were corrected for factors such as absorption and Lorentz- and polarization factor (LPA correction). The Diffraction Elastic Constants (DEC) S_1 and $\frac{1}{2}S_2$ required for the evaluation of the residual stresses and stress depth profiles are obtained by the Eshelby–Kröner model using single crystal

TABLE I. Experimental parameters for the X-ray residual stress study.

X-ray line	CuK α (without K β -filter) 40 kV/45 mA (long fine focus)
Optical elements	Primary beam: <i>polycapillar – semilens</i> diffracted beam: 0.4° <i>soller</i> slit +(001) LiF – <i>monochromator</i>
Studied reflection	Austenite 311
2θ -range	89° to 92.5°
Step width $\Delta 2\theta$	0.05°
Counting time	15 s/step
ψ -range	0° to 89.5°
Calibration	Au-powder

elastic constants for austenitic stainless steel.^{23,24} The calculated values are $S_1 = -1.77 \times 10^{-6} \text{ MPa}^{-1}$ and $\frac{1}{2}S_2 = 7.11 \times 10^{-6} \text{ MPa}^{-1}$. For the purpose of comparison, considering an isotropic material, the DEC's are given by $S_1 = -\nu/E$ and $\frac{1}{2}S_2 = (1 + \nu)/E$, where E and ν are the Young's modulus and the Poisson ratio, respectively.²⁵ Substituting S_1 and S_2 by the values calculated by the Eshelby–Kröner's model in the expressions of the DEC's for isotropic materials, the module of Young and the Poisson ratio are $E = 186 \text{ GPa}$ and $\nu = 0.3$, respectively, i.e., values compatible with the studied material.

As remarked above, residual stresses were calculated by applying two techniques. First, by means of the conventional $\sin^2 \psi$ -method^{22,26} the in-plane residual stress components σ_{11} and σ_{22} (direction 1 matches the direction of the ion beam projection on the bombarded samples) as well as the out-of-plane shear stresses components σ_{13} and σ_{23} were analyzed. Furthermore, by analyzing the lattice spacing d_{ψ}^{311} in the strain-free direction ψ^* of the biaxial residual stress state, which is defined by $\psi^* = \sin^{-1} \sqrt{-2S_1^{hkl} / \frac{1}{2}S_2^{hkl}}$, the near surface residual stress state was shown to be biaxial, i.e., the assumption $\sigma_{33} = 0$ is valid within the small range irradiated by the X-ray beam. Indeed, this is in agreement with the physical expected result that the free sample surface is allowed to relax. The value $\psi^* = 44.9^\circ$ is obtained by using the diffraction elastic constants S_1 and S_2 given above. Second, by analyzing the same set of X-ray measurements by the so-called *Universal Plot Method* (UPM),^{27,28} the depth profile of the stresses σ_{11} and σ_{22} components was evaluated (see the [Appendix](#)). Briefly, by performing X-ray diffraction in the ψ -mode (i.e., by tilting the sample around an axis in the diffraction plane), the X-ray diffraction bring information from a depth $\tau = \sin \theta \cos \psi / 2\mu$, where μ denotes the linear X-ray absorption coefficient of the sample.²⁷ Due to the exponential attenuation of the X-rays in the material, for any physical quantity $f(z)$ (e.g., strain), the X-ray diffraction yields *weighted averages* with respect to the depth $\tau = \sin \theta \cos \psi / 2\mu$ below the surface. In other words, the *averaged* value (mean value) of any depth-physical property $f(z)$ can be calculated by: $\langle f(\tau) \rangle = \int_0^\infty f(z) e^{-z/\tau} dz / \int_0^\infty e^{-z/\tau} dz$ where τ could be thought as an attenuation characteristic depth-length and the brackets stand to indicate an averaged value of the physical magnitude $f(z)$ weighted by the exponential $e^{z/\tau}$. Mathematically, this equation represents the “Laplace transform” of $f(z)$ to the τ space, normalized by the integral $\int_0^\infty e^{-z/\tau} dz$ of the weight function. Afterward, $f(z)$ can be obtained from the inverse Laplace transform \mathcal{L} , i.e., $f(z) = \mathcal{L}(\langle f(\tau) \rangle)$.^{22,28} Following this procedure, the stress distributions $\sigma_{11}(\tau)$ and $\sigma_{22}(\tau)$ curves are obtained (Equations (A6a) and (A6b), [Appendix](#)). For the real space profiles, we used an exponentially damped first order polynomial function to describe the depth distribution of the biaxial tensor stress components $\sigma_{ii}(z) = (a_0 + a_1 z) e^{-a_2 z}$ ($i = 1, 2$).²² The corresponding expression in the Laplace space (τ) is given by $\sigma_{ii}(\tau) = a_0 / (a_2 \tau + 1) + a_1 \tau / (a_2 \tau + 1)^2$ ($i = 1, 2$). Here z is the coordinate perpendicular to the sample's surface, with $z = 0$ at the surface and a_0 , a_1 , and a_2 are adjustable parameters.

III. RESULTS AND DISCUSSION

A. Surface morphology of bombarded samples

Figure 2 shows the morphology of Xe^+ bombarded AISI 316L samples. In the images, the axis “1” indicates the projection of ion beam direction on the sample surface employed during the bombarding experiments. In all cases, the ion bombardment evidenced the crystalline grains of the material and promoted the formation of peculiar patterns within those grains (ripples, grooves, dunes, terraces, and mounds).¹⁴ This behavior suggests a surface accommodation mechanism that depends on the crystalline orientation of individual grains, as expected in the *Ehrlich–Schwoebel instability model* for metals.^{4,5,7} Roughly speaking, according to the model, the regular pattern stems essentially from two mechanisms inducing surface instability. First, the sputtering yields dependence on the surface local curvature. Second, the surface energy barriers hinder adatoms to diffuse over step edges.⁸

The crystalline material structure is also important in the process. The non-directional bonds character in metals facilitates the accommodation of atoms and the ripples tend to follow the material crystalline orientation. Besides these general characteristics of the surface morphology, the presence of mounds aligned with the ion beam direction observed for $\nu = 60^\circ$ (Figure 2(e)) suggests that in some cases the

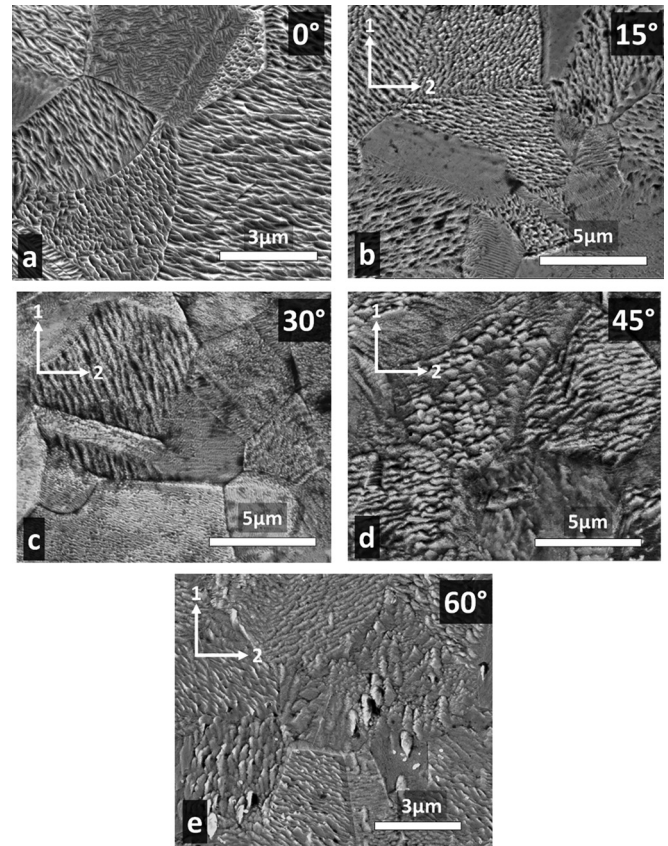


FIG. 2. SEM images of AISI 316L studied samples bombarded with Xe^+ using different ion impinging angles: (a) 0° (perpendicular bombardment); (b) 15° ; (c) 30° ; (d) 45° ; and (e) 60° at 1 keV fixed energy. Indicated *direction 1* (arrow) corresponds to the projection of the ion beam direction on the substrate.

formation of patterns is probably also related to ion momentum transfer.

B. Residual stress analyzed by the $\sin^2\psi$ -method

The $d_{\varphi\psi}^{311}$ vs $\sin^2\psi$ diagrams obtained for the studied samples (reference pristine and bombarded samples, respectively) are shown in Figure 3. Here $d_{\varphi\psi}^{311}$ is the standard nomenclature indicating the interplanar distance associated with the 311 direction (φ and ψ were defined in Section II B). The negative slope observed for all $d_{\varphi\psi}^{311}$ vs. $\sin^2\psi$ distributions and the absence of ψ -splitting indicate a compressive in-plane residual stress state and negligible shear stresses σ_{13} and σ_{23} . It is remarked that the pristine studied samples have compressive stress probably due to the polishing procedure²⁹ or the roll-forming manufacturing stainless steel sheet process. As observed in the plots, the $d_{\varphi\psi}^{311}$ vs. $\sin^2\psi$ diagrams obtained for the reference sample as well as for the perpendicularly bombarded one are nearly independent of the measured azimuthal angles φ . However, the plots for the bombarded samples under oblique ion incidence exhibit a larger negative slope for $\varphi=0^\circ$ and $\varphi=180^\circ$ as compared with those curves obtained at $\varphi=90^\circ$ and $\varphi=270^\circ$ azimuthal angles, respectively. Consequently, higher compressive stresses are present for the σ_{11} and σ_{22} component of the stress tensor. Finally, the plots for all samples show a non-linear behavior for the largest ψ values, indicating residual stress gradients.

Table II shows the absolute values of the in-plane residual stress components σ_{11} and σ_{22} obtained by the $\sin^2\psi$ -method. In the last column, the calculated lattice parameter values in

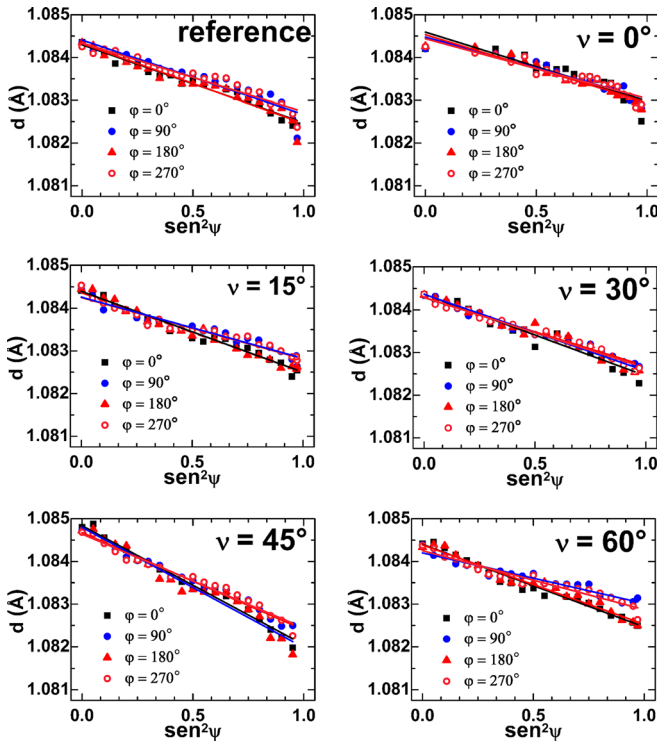


FIG. 3. $d_{\varphi\psi}^{311}$ vs. $\sin^2\psi$ plots for the reference and bombarded samples, at different measured azimuthal angles φ . The points correspond to the experimental information and the lines are linear regressions.

TABLE II. In-plane components of the residual stress tensor obtained for all the studied samples. The last column contains the calculated lattice parameters in the strain-free direction of the biaxial stress state, $a_{\psi^*}^{311}$.

Incident angle	σ_{11} (MPa)	σ_{22} (MPa)	$a_{\psi^*}^{311}$ (nm)
Reference	-277 ± 15	-259 ± 13	0.35937
0°	-231 ± 9	-203 ± 11	0.35935
15°	-248 ± 7	-192 ± 8	0.35933
30°	-259 ± 7	-244 ± 6	0.35933
45°	-380 ± 10	-320 ± 10	0.35935
60°	-237 ± 6	-165 ± 8	0.35938

the strain-free direction, $a_{\psi^*}^{311}$, are listed. They were obtained from the regression lines fitted to the $\sin^2\psi$ plots shown in Figure 3 in the strain-free direction of the biaxial stress state, $\psi^*,^{311} = 44.9^\circ$. Since all calculated $a_{\psi^*}^{311}$ values are very similar and close to the strain-free lattice parameter of austenitic steel, it can be concluded that the out-of-plane normal stress component σ_{33} can be neglected. The small uncertainties obtained for the individual stress values result from the almost linear $\sin^2\psi$ -data in Figure 3 and good fit by the regression line.

Figure 4 summarizes the dependence of the compressive stress as a function of the ion-impinging angle for the stress tensor components σ_{11} and σ_{22} . In this figure, we can see that the compressive stress presents a maximum for an ion impinging angle of $\sim 45^\circ$. It is worthy to call the attention that the shape of the curve displayed in Figure 4 resembles the sputter yield dependence on ion impinging angle, i.e., the sputtering yield displays a maximum around 45° (Figure 1). This observation suggests that the compressive stress is related with the sputter yield, i.e., with the mechanism of ion-substrate interaction that depends on the mass and energy of the incident projectile. If it is so, the maximum compressive stress is due, might be, to the maximum of energy transfer from the incoming ions to the substrate at $\sim 45^\circ$.³⁰

Moreover, according with the classical Sigmund's theory,⁴ the sputtering Yield is given by $Y(E, \theta) = K F_D(E, \nu, x=0)$, where K is a constant material dependent, F_D is a function depending on $\tilde{n}z$, the axis perpendicular to the plane $y-x$ contained on the assumed flat sample surface, ν is the ion incident angle measured relative to the normal \tilde{n} , and E is the energy of the initial impinging ion. The average energy deposited in a slab of volume $dV = x y dz$ is given by $F_D(E,$

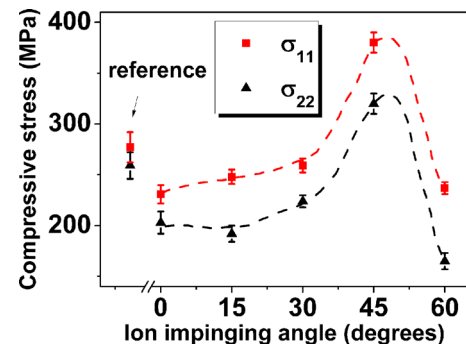


FIG. 4. Absolute stress values obtained by the $\sin^2\psi$ -method as a function of the ion impinging angle for the stress components σ_{11} and σ_{22} .

ν , z) dz . Focusing only on the angular dependence, Y is given by $Y(E, \nu, z=0) \sim (\cos \nu)^{-f}$, where $0 < f < 2$.⁴ Experimentally, the sputtering yield Y first increases monotonically on ν as given by the $(\cos \nu)^{-f}$ dependence. Afterward, Y decreases, defining a maximum which depends on the material and the fact that the surface is not perfectly flat.⁴ Moreover, this maximum depends also on smoothing mechanism, such as surface atoms diffusion and relocation by momentum transference.⁸ In fact, Figure 1 resembles this behavior, with a maximum around $\nu \approx 45^\circ$. Figure 4, also, shows the same peculiar effect at $\nu \approx 45^\circ$ which is associated with the sputtering yield behavior.

Figure 5 shows the difference between the absolute values of biaxial stress tensor components $\sigma_{11} - \sigma_{22}$ as a function of ion impinging angle. These results show that the samples exposed to tilted bombardment present higher compressive stress in the *direction of the projected ion beam* on the sample surface. Moreover, the difference between σ_{11} and σ_{22} increases on ion impinging angles for the studied oblique incidence range. This difference is probable due to the effect of momentum transferred to the sample atoms in the direction of the incoming xenon ions. Therefore, the knock-on implantation phenomenon causes higher compressive stress mainly along this direction.¹⁶

C. Residual stresses gradients

As evidenced in Section III B, the $d_{\phi\psi}^{311}$ vs. $\sin^2\psi$ plots are not linear suggesting the existence of in depth stress gradients perpendicular to the sample surface. Therefore, in order to determine the depth distribution of the components of the stress tensor, the same sets of X-ray diffraction data were analyzed applying the formalism outlined in Section II B (see more detail in the Appendix). For this purpose, we assumed an exponentially damped first order polynomial function to describe the distributions of σ_{11} and σ_{22} (see Section II B). Figure 6 shows the in-plane biaxial stress components σ_{11} and σ_{22} depth profiles. The plots show that the surface is under compressive stress between ~ -200 MPa and ~ -400 MPa, relaxing on increasing depth z . We noted the strong scattering of the discrete Laplace stress data in those τ -regions corresponding to the vicinity of the strain-free direction ψ^* (see square gray regions, Figure 6) as well as at small ψ -angles (near to the surface, Figure 6). We

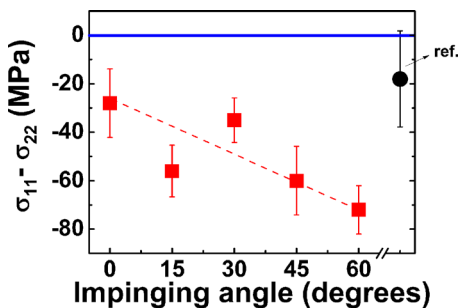


FIG. 5. Difference between stress tensor components σ_{11} and σ_{22} as a function of the impinging angle. Blue line marks where the difference is zero (equal components) and the circle point shows the difference value for the reference sample. The dashed line is a guide for the eyes.

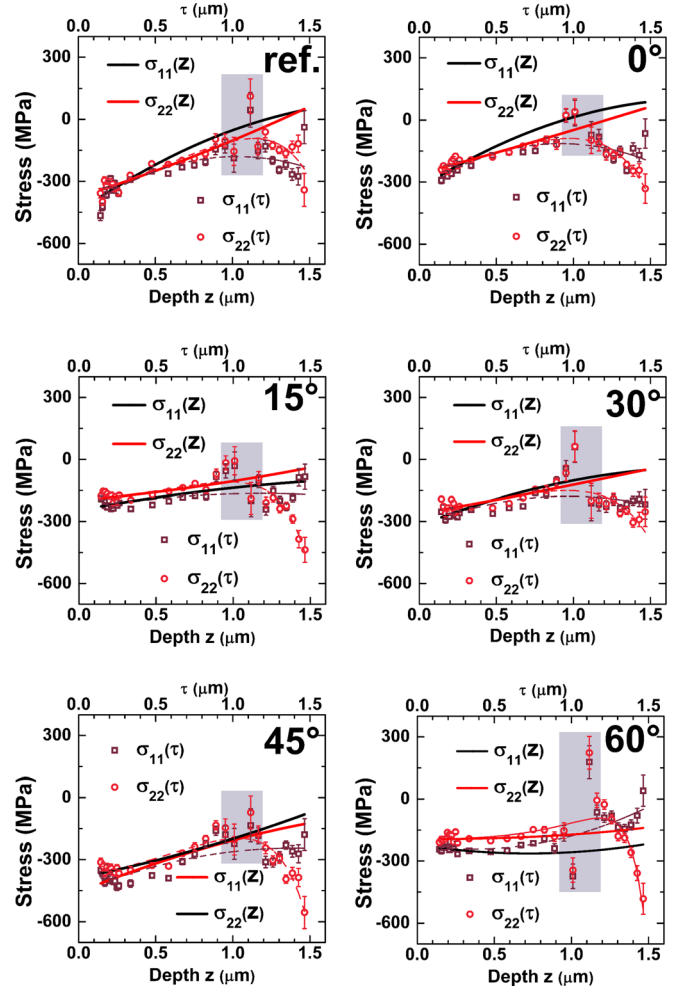


FIG. 6. Results obtained from the “Universal Plot Method” for the reference and bombarded samples at different impinging angles. The plots show discrete Laplace values $\sigma_{11}(\tau) - \sigma_{22}(\tau)$ (squares and circles, respectively) as well as the correspondent fitting functions (dashed lines). Real space profiles $\sigma_{11}(z) - \sigma_{22}(z)$ (solid lines) were obtained by Laplace transform from $\sigma_{11}(\tau) - \sigma_{22}(\tau)$. The gray areas mark regions of strong scattering of the discrete Laplace stress data in the space τ , corresponding to the strain-free direction. Here, τ is an X-ray attenuation characteristic depth-length.²⁷ See text for further details.

should remark that this data dispersion stems from the stress evaluation formalism applied within the framework of the *universal plot method* (Appendix). From the Equations (A5a) and (A5b) is obtained that both the numerator and the denominator become very small in the aforementioned ψ -regions, leading to disperse data results. Therefore, the corresponding stress values have larger uncertainties and, consequently, are responsible for the larger experimental error obtained by the least squares fit procedure.

Comparing the graphs on Figure 6, we can see that the in-depth stress profile depends on the ion-impinging angle. Near to the surface ($\sim 0.5 \mu\text{m}$ depth), one can see that stress distributions for bombarded samples (excepting 45°) are less compressive than the one measured for pristine samples. The origin of this effect is uncertain because two different phenomena must be taken into account. First, thermal spikes due to the ion impact reduce stress by providing sufficient energy to the neighbor’s atoms that eventually merge to the surface. Second, the ion bombardment removal of the topmost

stressed atomic layers modifies the original surface, preventing any valuable comparison (Figure 1), i.e., the coordinate of the sample surface $z=0$ of the reference sample does not coincide with those of the treated samples. However, Figure 5 shows a marked biaxial stress asymmetry of the bombarded samples on the ion impinging angle, virtually absent in the reference sample (Figure 5), i.e., the observed results are due exclusively to the ion bombarding treatment.

In bulk (depths beyond $1\ \mu\text{m}$), tilted bombardment induced compressive stress for all samples, a phenomenon ascribed to the knock-on process.¹⁶ Indeed, as mentioned above, the ion momentum transfer to the substrate depends on the bombarding angle and thus the induced underneath biaxial stress (Figure 4). We note, also, that in spite of the different residual stress values found after bombardment, the main features of the surface patterns as a function of ion incidence angle are maintained (see Figure 2). However, more work is necessary in order to understand the effect of both the residual stress as well as of the angle of ion bombarding on the patterns formation.

Finally, it is interesting to compare our results with those obtained by other researchers. Dahmen *et al.*³¹ studied the influence of the ion bombarding on the stress of Cu foils by measuring the samples curvature as a function of the dose. The technique used by these researchers is based in the curvature prompted in the sample by the ion bombarding. As remarked by the authors, this technique provides an average stress of the affected region by the ions since there is no discrimination on depth and strain asymmetries. With the purposes of comparison, one can estimate the average value of the stress obtained in our experiments. Let us assume $t \sim 10\ \text{nm}$, the region considered by Dahmen *et al.* in the stress calculation affected by the ion bombarding. Also, taking at the surface the stress value $\sim -300\ \text{MPa}$ in our samples, we can obtain the “stress thickness” given by the Stoney³² equation $\langle \tau \rangle = \int_0^t \sigma dx - \langle \sigma \rangle t \approx -300\ \text{MPa} \times 10\ \text{nm} = -3\ \text{N/m}$, where it was assumed that the stress is approximately constant in the thin slab of thickness t . Although there is not a straightforward comparison with our results, this estimation is of the order of the value obtained by the cited authors bombarding Cu with $800\ \text{eV Ar}^+$ ions. Similar results were also reported by Chan *et al.*³³

IV. CONCLUSIONS

This work reports the influence of Xe^+ ion bombarding angle on the residual stress of polycrystalline iron alloy (AISI 316L stainless steel) samples. Results obtained from X-ray diffraction measurements applying the $\sin^2\psi$ -method showed that all the studied samples display in-plane biaxial compressive stress, with higher values along the direction of the projected ion beam on the bombarded surface. Moreover, the difference $(\sigma_{11} - \sigma_{22})$ of the stress tensor biaxial components increases on ion impinging angles, phenomenon associated with the knock-on implantation, i.e., higher momentum transference along the direction of the projected ion beam on the sample surface. The analysis of the X-ray measurements shows that the process of ion bombarding does not prompt shear stress. The in-depth state of stress of

the pristine samples shows higher biaxial compressive stresses near to the surface than the bombarded ones. This is probably due to the polishing procedure or the roll-forming manufacturing stainless steel sheet process. The origin of these findings is probably due to the following causes: (1) thermal spikes prompted by the ions bombarding, and (2) sputtering of the topmost atomic material layers. The former reduces the stress by augmenting the mobility of implanted ion neighbor’s atoms that eventually will move enough distance as to reach the surface, relaxing the material. The latter one is due to the ion erosion of the topmost material layers originally more stressed.

Finally, we note that the effect of the ion bombarding extends a depth deeper than the ion penetration, estimated in $\sim 1\text{--}1.8\ \text{nm}$, phenomenon due to knock-on effect. Although without quantitative information, we note that the different stresses observed in the bombarded samples seem to not affect significantly the formation of patterns, i.e., the main characteristic of the surface morphology after bombardment (patterns confined within the crystalline grains) remains similar for all the studied cases. This observation suggests that the ripples formation is mainly an atomic property of the metallic bonding character of the studied material.

ACKNOWLEDGMENTS

Part of this work was supported by FAPESP, Project No. 2012/10127-5. S.C., C.A.F., and F.A. are CNPq fellows. SEM images were obtained at the Brazilian Nanotechnology National Laboratory, Campinas, SP (LNNano). The authors are grateful to Dr. D. Apel and Dr. M. Meixner for their help in the stress measurements and to C. Piacenti for technical help.

APPENDIX: THE “UNIVERSAL PLOT METHOD” (UPM)

By performing the X-ray diffraction in the ψ -mode (i.e., by tilting the sample around an axis in the diffraction plane), the X-ray diffraction information comes from a depth $\tau = \sin\theta \cos\psi/2\mu$, where μ denotes the linear X-ray absorption coefficient.^{22,27} Due to the exponential attenuation of the X-rays in the material, for any physical quantity $f(z)$ (e.g., stress or strain), the X-ray diffraction yields *weighted averages* of $\langle f(z) \rangle$ with respect to the depth τ below the surface. In other words, the *averaged* value (mean value) of any depth-physical property $f(z)$ can be calculated by

$$f(\tau) \equiv \langle f(\tau) \rangle = \int_0^\infty f(z) e^{-z/\tau} dz / \int_0^\infty e^{-z/\tau} dz, \quad (\text{A1})$$

where τ is an attenuation characteristic depth-length and the brackets stand to indicate an averaged value of the physical magnitude $f(z)$ weighted by the exponential $e^{z/\tau}$. Mathematically, this equation represents the “Laplace transform” of $f(z)$ to the τ space normalized by the integral $\int_0^\infty e^{-z/\tau} dz$. Afterward, $f(z)$ can be obtained from the inverse Laplace transform \mathcal{L} , i.e., $f(z) = \mathcal{L}(\langle f(\tau) \rangle)$. Particularly, in terms of the lattice strains and residual stresses, the expressions for these quantities as a function of τ are^{22,28}

$$\varepsilon_{\varphi\psi}^{hkl}(\tau) = \int \varepsilon_{\varphi\psi}^{hkl}(z) e^{-z/\tau} dz / \int e^{-z/\tau} dz, \quad (\text{A2a})$$

$$\sigma_{ij}(\tau) = \int \sigma_{ij}(z) e^{-z/\tau} dz / \int e^{-z/\tau} dz, \quad (\text{A2b})$$

where $\sigma_{ij}(z)$ and $\varepsilon_{\varphi\psi}^{hkl}(z)$ are obtained from the inverse Laplace transform of the $\sigma_{ij}(\tau)$ and $\varepsilon_{\varphi\psi}^{hkl}(\tau)$ profiles.

For a biaxial state of stress, the fundamental equation takes the following depth-dependent form:

$$\varepsilon_{\varphi\psi}^{hkl}(\tau) = F_{11}^{hkl}(\varphi, \psi) \sigma_{11}(\tau) + F_{22}^{hkl}(\varphi, \psi) \sigma_{22}(\tau), \quad (\text{A3})$$

where F_{ij}^{hkl} are the so-called stress factors which are given by the equations

$$F_{11}^{hkl}(\varphi, \psi) = \frac{1}{2} S_2^{hkl} \cos^2 \varphi \sin^2 \psi + S_1^{hkl}, \quad (\text{A4a})$$

$$F_{22}^{hkl}(\varphi, \psi) = \frac{1}{2} S_2^{hkl} \sin^2 \varphi \sin^2 \psi + S_1^{hkl}, \quad (\text{A4b})$$

where S_1 and $S_2/2$ are diffraction elastic constants.²² Equation (A3) can be solved for the unknown depth profiles $\sigma_{11}(\tau)$ and $\sigma_{22}(\tau)$. Writing

$$f^+(\tau) = \left[\varepsilon_{0\psi}^{hkl}(\tau) + \varepsilon_{90\psi}^{hkl}(\tau) \right] / \left(\frac{1}{2} S_2^{hkl} \sin^2 \psi + 2S_1^{hkl} \right), \quad (\text{A5a})$$

$$f^-(\tau) = \left[\varepsilon_{0\psi}^{hkl}(\tau) - \varepsilon_{90\psi}^{hkl}(\tau) \right] / \left(\frac{1}{2} S_2^{hkl} \sin^2 \psi \right), \quad (\text{A5b})$$

yields the in-plane stress in the τ space, exclusively depending on the experimental raw

$$\sigma_{11}(\tau) = \frac{1}{2} [f^+(\tau) + f^-(\tau)], \quad (\text{A6a})$$

$$\sigma_{22}(\tau) = \frac{1}{2} [f^+(\tau) - f^-(\tau)]. \quad (\text{A6b})$$

In order to get the actual stress depth profile in the real or z-space, $\sigma_{11}(z)$ and $\sigma_{22}(z)$, the experimentally obtained Laplace stress distribution $\sigma_{11}(\tau)$ and $\sigma_{22}(\tau)$ given by Equation (A6) is usually fitted by polynomial or exponential functions.²² Afterwards, the stress depth profiles $\sigma_{11}(z)$ and $\sigma_{22}(z)$ are obtained from the Laplace transform of the fitted functions by means of Equation (A2).

- ¹W. P. Tong, N. R. Tao, Z. B. Wang, J. Lu, and K. Lu, *Science* **299**, 686 (2003).
- ²G. Abrasonis, R. Gago, I. Jimenez, U. Kreissig, A. Kolitsch, and W. Möller, *J. Appl. Phys.* **98**, 074907 (2005).
- ³P. Willke, J. A. Amani, A. Sinterhauf, S. Thakur, T. Kotzot, T. Druga, S. Weikert, K. Maiti, H. Hofsass, and M. Wenderoth, *Nano Lett.* **15**, 5110 (2015).
- ⁴P. Sigmund, *Phys. Rev.* **184**, 383 (1969).
- ⁵W. L. Chan and E. Chason, *J. Appl. Phys.* **101**, 121301 (2007).
- ⁶E. A. Ochoa, C. A. Figueroa, and F. Alvarez, *Surf. Coat. Technol.* **200**, 2165 (2005).
- ⁷U. Valbusa, C. Boragno, and F. Buatier de Mongeot, *J. Phys.: Condens. Matter* **14**, 8153 (2002).
- ⁸R. M. Bradley and J. M. E. Harper, *J. Vac. Sci. Technol. A* **6**(4), 2390 (1988).
- ⁹R. M. Bradley, *Phys. Rev. B* **87**, 205408 (2013).
- ¹⁰G. Abrasonis, W. Möller, and X. X. Ma, *Phys. Rev. Lett.* **96**, 065901 (2006).
- ¹¹E. A. Ochoa, C. A. Figueroa, T. Czewiec, and F. Alvarez, *Appl. Phys. Lett.* **88**, 254109 (2006).
- ¹²E. A. Ochoa, R. Droppa, R. L. O. Basso, M. Morales, S. Cucatti, L. F. Zagonel, T. Czewiec, M. C. dos Santos, C. A. Figueroa, and F. Alvarez, *Mater. Chem. Phys.* **143**, 116 (2013).
- ¹³K. Nakasa, A. Yamamoto, R. Wang, and T. Sumomogi, *Surf. Coat. Technol.* **272**, 298 (2015).
- ¹⁴S. Cucatti, E. A. Ochoa, M. Morales, R. Droppa, Jr., J. Garcia, H. C. Pinto, L. F. Zagonel, D. Wisnivesky, and F. Alvarez, *Mater. Chem. Phys.* **149–150**, 261 (2015).
- ¹⁵S. Uhlmann, Th. Frauenheim, and Y. Lifshitz, *Phys. Rev. Lett.* **81**, 641 (1998).
- ¹⁶C. A. Davis, *Thin Solid Films* **226**, 30 (1993).
- ¹⁷R. G. Lacerda, P. Hammer, F. L. Freire, F. Alvarez, and F. C. Marques, *Diamond Relat. Mater.* **9**, 796 (2000).
- ¹⁸E. Chason and P. R. Guduru, *J. Appl. Phys.* **119**, 191101 (2016).
- ¹⁹W. L. Chan, K. Zhao, N. Vo, Y. Ashkenazy, D. G. Cahill, and R. S. Averback, *Phys. Rev. B* **77**, 205405 (2008).
- ²⁰P. Hammer, N. M. Victoria, and F. Alvarez, *J. Vac. Sci. Technol. A* **16**, 2941 (1998).
- ²¹J. P. Biersack and L. G. Haggmark, *Nucl. Instrum. Methods* **174**, 257 (1980).
- ²²M. Birkholz, P. F. Fewster, and C. Genzel, *Thin Film Analysis by X-Ray Diffraction* (Wiley-VCK Verlag GmbH & CO. KGaA, Weinheim, 2006).
- ²³J. D. Eshelby, *Proc R. Soc. London, Ser. A* **241**, 376 (1957).
- ²⁴E. Kröner, *Z. Phys.* **151**, 504 (1958).
- ²⁵A. C. Vermeulen, *Adv. X-ray Anal.* **44**, 128 (2001).
- ²⁶E. Macherauch and P. Müller, *Z. Angew. Phys.* **13**, 305 (1961).
- ²⁷H. Ruppertsberg, I. Detemple, and J. Krier, *Phys. Status Solidi A* **116**, 681 (1989).
- ²⁸Ch. Genzel, *Phys. Status Solidi A* **146**, 629 (1994).
- ²⁹A. Ben Rhouma, C. Braham, M. E. Fitzpatrick, J. Lédon, and H. Sidhom, *J. Mater. Eng. Perform.* **10**(5), 507 (2001).
- ³⁰B. Chapman, *Glow Discharge Processes: Sputtering and Plasma Etching* (Wiley-Interscience, 1980).
- ³¹K. Dahmen, M. Giesen, J. Ikononov, K. Starbova, and H. Ibach, *Thin Solid Films* **428**, 6 (2003).
- ³²G. G. Stoney, *Proc. R. Soc. London, Ser. A* **82**, 172 (1909).
- ³³W. L. Chan, E. Chason, and C. Iamsumang, *Nucl. Instrum. Methods Phys. Res., Sect. B* **257**, 428 (2007).